Journal of Magnetism and Magnetic Materials 562 (2022) 169761

Contents lists available at ScienceDirect

Journal of Magnetism and Magnetic Materials

journal homepage: www.elsevier.com/locate/jmmm

Research article

Photoluminescence and magnetic properties of $SrMoO_4$ phosphors submitted to thermal treatment and electron irradiation

Roseli Künzel [a], Carla M. Santos Feldhaus [b], Yanna Oliveira Fancio Suzuki [b], Fabio Furlan Ferreira [c], Vinicius Gomes de Paula [c], Lilia C. Courrol [a], Nancy K. Umisedo [d], Elisabeth Mateus Yoshimura [d], Emico Okuno [d], Ana Paula de Azevedo Marques [b,*]

[a] *Universidade Federal de São Paulo - UNIFESP, Departamento de Física, R. São Nicolau, 210, Diadema SP, 09913-030, Brazil*
[b] *Universidade Federal de São Paulo - UNIFESP, Departamento de Química, R. São Nicolau, 210, Diadema SP, 09913-030, Brazil*
[c] *Universidade Federal do ABC, Santo André, 09210-580, SP, Brazil*
[d] *Universidade de São Paulo, Instituto de Física, Cidade Universitária, 05508-900, São Paulo, SP, Brazil*

ARTICLE INFO

Keywords:
Microwave processing
Ceramics
Optical properties
Magnetic property
Structural defects

ABSTRACT

The present work reports a systematic study on the effects of the synthesis methodology and post-synthesis treatments on the optical and magnetic properties of $SrMoO_4$ phosphors. The powders were prepared through co-precipitation (SMO1) and co-precipitation processed in a microwave-hydrothermal system (SMO2), with some of them submitted to heat treatment and beta particles irradiation. The irradiation and heat treatment affected SMO1 and SMO2 structures differently, but without modifying the scheelite type crystalline phase. The Rietveld refinement, Raman, FTIR data, and the TEM images indicated that the SMO1 samples are more disordered than SMO2, where the MHA treatment promotes higher-ordered materials. Under 280 nm and 359 nm excitation, the PL profile and intensity at room temperature are directly related to the sample order. Magnetization results confirm room temperature ferromagnetism for as-prepared and irradiated SMO1 samples with a magnetic moment of 0.15 and 0.05 emu/g, respectively. The as-prepared SMO2 sample shows diamagnetic behavior, and the SMO2 1.2 Gy sample presents a ferromagnetic response with a saturation magnetic moment of approximately 0.005 emu/g. The ferromagnetic behavior disappears after the heat treatment. Our results highlight the role of the density and distribution of structural defects such as oxygen vacancies in triggering ferromagnetism in $SrMoO_4$ compounds. The findings of this study reveal that the magnetic properties of the $SrMoO_4$ are susceptible to the preparation conditions and post-synthesis treatments. The coalescence of magnetic and optical properties in the $SrMoO_4$ compounds demonstrates that the properties of the samples can be modulated through synthetic methods or external influences, making it a viable candidate for several technological applications, including optoelectronic devices.

1. Introduction

Molybdates with general formulae $AMoO_4$ (A = Ba, Sr, Ca, and others) comprise a remarkable class of ceramic materials that exhibit distinct functional properties [1,2]. $SrMoO_4$ crystallizes in the scheelite structure pertaining to the tetragonal space group $I4_1/a$ [3]. The $SrMoO_4$ compounds exhibit outstanding luminescence output at room temperature and have found importance in the optoelectronic [4], gas sensor [5,6], optical devices [7–9], catalysts [10], and scintillation detectors [11,12]. The remarkable structural properties, emerging from different synthesis methodologies and treatments, affect the properties of the materials and provide a strong motivation towards reaching a deep understanding of $SrMoO_4$ behavior.

The crystallization process, particle size, and particle morphology highly determine the optical, electrical, magnetic, and mechanical properties of the nanoparticles. Regarding $SrMoO_4$ optical properties, it is a broadband phosphor, with the photons emission occurring from the red to the blue spectral region. Optical emissions are believed to be related to electronic transitions of the $[MoO_4]^{2-}$ complexes and defect centers present in the material [9,13–15]. The photoluminescence spectra registered in molybdates give insight that recombination in deep hole defects is responsible for the green, yellow, orange, and red wavelength photons emissions, while shallower hole recombination produces the blue and violet emissions at room temperature [16]. The light output efficiency and emission profile depend on the concentration and distribution of surface defect states [9,17]. The luminescence

---

* Corresponding author.
E-mail address: apamarques@unifesp.br (A.P. de Azevedo Marques).

https://doi.org/10.1016/j.jmmm.2022.169761
Received 17 November 2021; Received in revised form 19 July 2022; Accepted 24 July 2022

behavior of scheelite structured $SrMoO_4$ compounds is extensively studied in the literature, whereas few reports investigate their magnetic properties.

The origin of unexpected magnetism at room temperature identified in unconventional materials, which have entirely empty or full d and f bands, have attracted great deal of interest in the scientific community [18]. The unusual magnetic behavior has been associated with the reduced dimensions of particles, the distance between atoms, structural disorder, and defects, including oxygen vacancies [19–24]. In the case of oxygen vacancies, they can provoke the exchange interaction between the spins of unpaired electrons present at the nanoparticle surface [18,25]. The ferromagnetic order at room temperature was also observed in some non-magnetic undoped molybdates, including $BaMoO_4$ and $SrMoO_4$ [25–27]. $SrMoO_4$ samples synthesized by the sonochemical method display ferromagnetic performance at room temperature [26]. Muralidharan et al. (2016) synthesized $SrMoO_4$ powders by the chemical precipitation method and reported that $SrMoO_4$ powders, with 4.36 eV band gap, display paramagnetic behavior while the $SrMoO_4$ samples doped with Cr ions show ferromagnetic behavior [22]. Recently, Muralidharan and Sivaji (2020) synthesized $SrMoO_4$, by the chemical precipitation method, with 4.25 eV band-gap, and observed the occurrence of ferromagnetic ordering at room temperature attributed to oxygen vacancies [25]. The degree of the lattice structural order–disorder affects the intermediary energy levels density and position, impacting the band gap energy value. These defects states within the band gap can be induced by impurities, oxygen vacancies, or distortions of the $[MoO_4]$ tetrahedron. The concentration and distribution of the intermediary energy levels are extremely sensitive to the conditions and synthesis method, and the applied post-synthetic treatments used to tune defects in a controllable way in the samples, such as heat treatment or ion beam irradiation [23]. Many works in the literature reported on the dependence of ferromagnetism ordering with the defect distribution and density in several compounds [23], and to our present body of knowledge, these aspects remain unknown for $SrMoO_4$ compounds. In this work, we investigate the structural, morphological, optical, and magnetic properties of $SrMoO_4$ powders synthesized by co-precipitation and co-precipitation followed by the MAH method. In order to achieve distinct defects density and distribution, the samples were submitted to thermal treatment and irradiation with beta particles.

2. Materials and methods

2.1. Synthesis and treatments of the $SrMoO_4$ powders

Molybdenum trioxide (MoO_3) (Alfa Aesar, 99.95%), strontium acetate

($(CH_3CO_2)_2Sr$) (Alfa Aesar, 99%), KOH and distilled water were used to synthesize the $SrMoO_4$ powders. As described in our previous works, the samples were synthesized using the co-precipitation method [9,17]. The methodology can be described as follows: 5×10^{-3} mol of MoO_3 was dissolved in approximately 50 mL of distilled water under vigorous stirring. After 5×10^{-3} mL of $(CH_3CO_2)_2Sr$ was added under constant stirring, and KOH was employed to adjust the pH of the solution to 12. For the SMO1 sample, the solid precipitate was collected, washed with water and ethanol, and dried at 60° C. In the case of the SMO2 sample an additional Microwave-Assisted Hydrothermal (MAH) treatment was employed. The synthesis and treatment procedures for each sample are illustrated in Fig. 1

Irradiation with beta particles and heating treatments were employed to obtain SMO1 and SMO2 samples with different degrees of defects density and distribution. The as-prepared SMO1 and SMO2 powders were exposed to a dose of 1.2 Gy from a $^{90}Sr/^{90}Y$ beta particles source with an activity of 1.48 GBq build-in a Risø TL/OSL reader, model DA-20. SMO1 and SMO2 samples were also irradiated with 1.2 Gy beta particles followed by two consecutive heating cycles at a constant heating rate (3 K/s) from room temperature to 873 K during a thermoluminescence readout in the TL/OSL system [17]. An as-prepared sample of SMO1 and SMO2 powders were submitted to a heating process at a constant heating rate (0.5 K/s) from room temperature to 873 K. Henceforward in this paper, the SMO samples will be identified by the codes provided in Table 1.

Table 1
$SrMoO_4$ (SMO) sample code, absorbed dose due to irradiation with beta particles and heat treatment. SMO1 stands for samples produced by co-precipitation and SMO2 for samples produced by co-precipitation and submitted to microwave-assisted hydrothermal (MAH).

Sample				
Name	Absorbed Dose (mGy)	TL readout until 873 K	Heating rate (K/s)	number of heating cycles
SMO1				
as-prepared	0	No	––	––
1.2 Gy	1.2	No	––	––
1.2 Gy + 3 K/s	1.2	Yes	3	2
0.5 K/s	0	Yes	0.5	1
3 K/s	0	Yes	3	2
SMO2				
as-prepared	0	No	––	––
1.2 Gy	1.2	No	––	––
1.2 Gy + 3 K/s	1.2	Yes	3	2
0.5 K/s	0	Yes	0.5	1
3 K/s	0	Yes	3	2

2.2. Characterization of $SrMoO_4$ samples

X-ray diffraction (XRD) data were recorded using a transmission geometry on a STADI-P diffractometer (STOE&Cie GmbH) with $CuK\alpha_1$ radiation (λ = 1.54056 Å) with a curved Ge(111) crystal, using a voltage of 40 kV and a current of 40 mA. The Rietveld method was employed to refine the structural parameters, and peak profiles of the XRD patterns [28–30] using the TOPAS-Academic v7 software [31]. A modified Thompson Cox–Hasting pseudo-Voigt (TCHZ) function [32] was used to model the peak shapes of a standard silicon sample from the National Institute of Standards and Technology (NIST, SRM640c). The refined values for the Gaussian and Lorentzian contributions were then kept fixed. In this sense, the apparent crystallite sizes and microstrain contributions could be deconvoluted from the instrumental contribution. The crystallite sizes were calculated using the integral breadth based LVol macro, as described in the TOPAS-Academic v7 Technical reference manual [33].

A Renishaw microscope (in Via model) with a multichannel CCD detector and He–Ne laser (632.8 nm) was employed to register the Raman spectra ranging from 80 cm^{-1} to 1000 cm^{-1}. The automatic cosmic ray removal option was set on. A Shimadzu IRPrestige-21 spectrophotometer was employed to register the Fourier Transformed Infrared spectra (FTIR) in the spectral range from 500 to 1000 cm^{-1}. The absorbance measurements were carried on a Shimadzu UV-2600 spectrophotometer in the wavelength range from 200 to 800 nm and spectral resolution of 0.1 nm. In wavelength units, the UV–Vis absorbance spectra were converted to energy scale using the Jacobian Conversion method [34]. The band gap energy was calculated employing the Tauc relation [35,36]. The particles morphology and the effect of the treatments were observed using a scanning electron microscope, SEM (Jeol JSM-6610LV). High-magnification imaging of the materials was carried out using transmission electron microscopy (TEM) using a Phillips CM120 microscopy, with a LaB6 filament and 200 kV accelerating voltage.TEM specimens were prepared on copper grids (TED PELLA, type B, 400 mesh). A small amount of powder was first dispersed in an isopropanol solution and immersed in an ultrasonic bath during 10 min to obtain a better dispersion. Finally, a drop of this dispersion was placed on a copper grid and dried at room temperature.

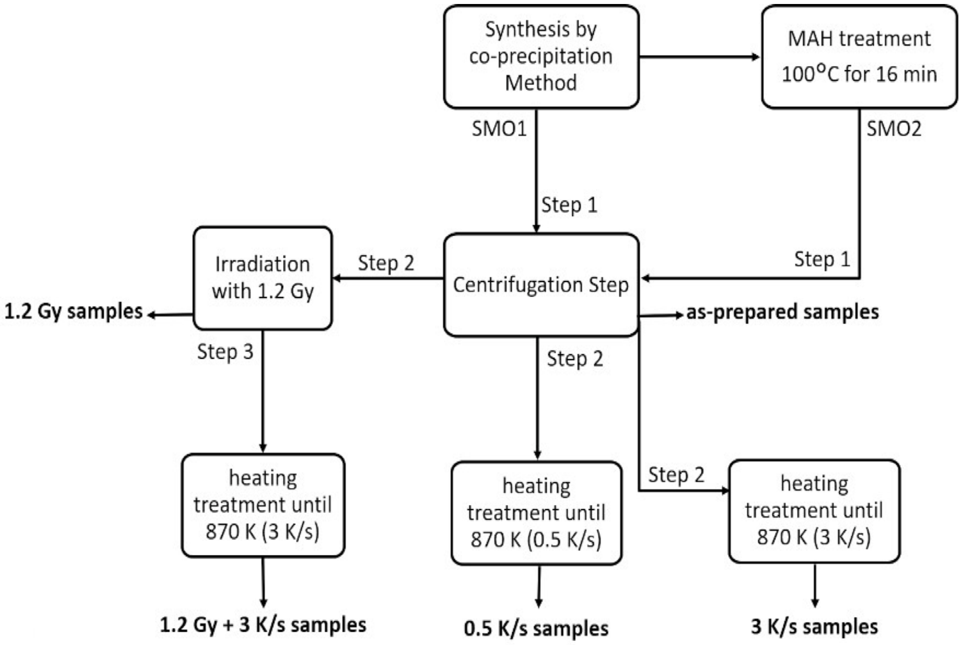

Fig. 1. Synthesis and post-synthesis treatments for each SMO1 and SMO2 sample.

The photoluminescence measurements were performed using a Fluorolog 3–11 spectrometer (HORIBA Jobin-Yvon, Longjumeau, France) coupled with a 450 W xenon arc lamp. The photoluminescence excitation (PLE) spectra was recorded for emission at 469 nm in the excitation range from 250–440 nm. The photoluminescence (PL) spectra were registered for wavelengths between 300–548 nm under 280 nm excitation, and 400–670 nm under excitation at 359 nm. The photoluminescence spectrum was recorded employing a bifurcated fiber optical outside the equipment. One fiber provides the sample excitation, and the other fiber collects the emission signal. The fiber bundle was placed vertically at about 2 mm of distance from the sample. The sample holder spectrum was subtracted from the spectrum recorded for each sample.

The magnetization as a function of the applied field was measured at room temperature using a superconducting quantum interference equipment magnetometer (MPMS SQUID magnetometer, Quantum Design Inc.) under applied magnetic fields up to 10 kOe. The powder samples were properly manipulated using plastic gloves and plastic tools to avoid contamination by magnetic impurities. Each sample was put inside gelatin capsules and loaded into plastic straws; this set was then attached to the end of a vertical rod and inserted into the equipment.

3. Results and discussion

3.1. Structural analysis

Fig. 2 shows the experimental XRD data compared with the results from the Rietveld refinement method for the SMO1 and SMO2 samples subjected to irradiation with beta particles and to thermal treatments (Table 1). The observed $SrMoO_4$ peaks for all samples could be indexed to the scheelite-type tetragonal structure with a space group of $I4_1/a$, which is in full agreement with the Bragg peaks provided in the JCPDS 08-0482 card [9,17]. The green line indicates that the difference between the experimental XRD pattern profiles and the theoretically calculated profiles are near zero in the intensity scale, as illustrated in Fig. 2. The Rietveld method was employed to estimate the lattice parameters and crystallite sizes, as well as quantitative phase analysis [37] to estimate the mass fractions of the observed phases, and the results are shown in Table 2. From the Rietveld refinement analysis, it was observed that all the samples display two additional peaks with very low intensities located at $2\theta = 25.25°$ and $2\theta = 25.9°$, assigned to strontium carbonate ($SrCO_3$) (JCPDS card no. 05-0418) [38,39]. These peaks probably result from the synthesis process or by the adsorption of the CO_2 molecule from the air by the defects present at the particles surface [40–42]. However, the origin of the $SrCO_3$ peaks observed in the $SrMoO_4$ diffractogram requires further investigation. The data of mass fractions of $SrCO_3$ and $SrMoO_4$ suggest that surface of the as-prepared SMO1 sample (designed without MHA) exhibits a higher disordered surface than the as-prepared SMO2 sample (processed with MHA). The higher degree of surface disorder favors the CO_2 adsorption. This fact indicates that the MHA process increases the surface order. The calculated lattice parameters show discrete modifications for the irradiated and heated treated samples. The unit cell volume discreetly decreases for the samples submitted to heat treatment (SMO 0.5 K/s and 1.2 Gy + 3 K/s) and increases for the irradiated samples (SMO 1.2 Gy). The change is minimum, which confirms the stability of the scheelite phase even after the irradiation with beta particles and heating treatment. By calculating the crystallite size of as-prepared SMO1 and SMO2, we observed that MHA treatment promotes the formation of smaller crystals (42%). The increase in the pressure of the MHA system favors the formation of more compact crystallites. In addition, the use of microwaves generates a higher organization level of the crystals through the molecular rotational vibrations caused by microwaves. Otherwise, the SMO2 0.5 k/s samples submitted to heat treatment display increased crystallite size compared to the SMO2 as-prepared sample around 60%, becoming similar to those observed for the as-prepared SMO1 sample with a difference of about 6%. During the heating process, many crystallites of a similar orientation join together to promote crystallite growth [43]. The crystallite size decreases for the irradiated SMO1 1.2 Gy sample and increases for the irradiated SMO2 1.2 Gy sample relative to their respective as-prepared samples. Therefore, irradiation with beta particles can either promote or impair the material order, depending on the material's previous degree of organization level. The unit cell parameters of the SMO1 and SMO2 samples are slightly lower than those of the standard value (JCPDS No. 08-0482), which indicates that both as-prepared SMO1 and SMO2 samples present a certain level of disorder degree. The observed distortion on the crystal structure can be associated with intrinsic defects such as oxygen vacancy, interstitial strontium ions,

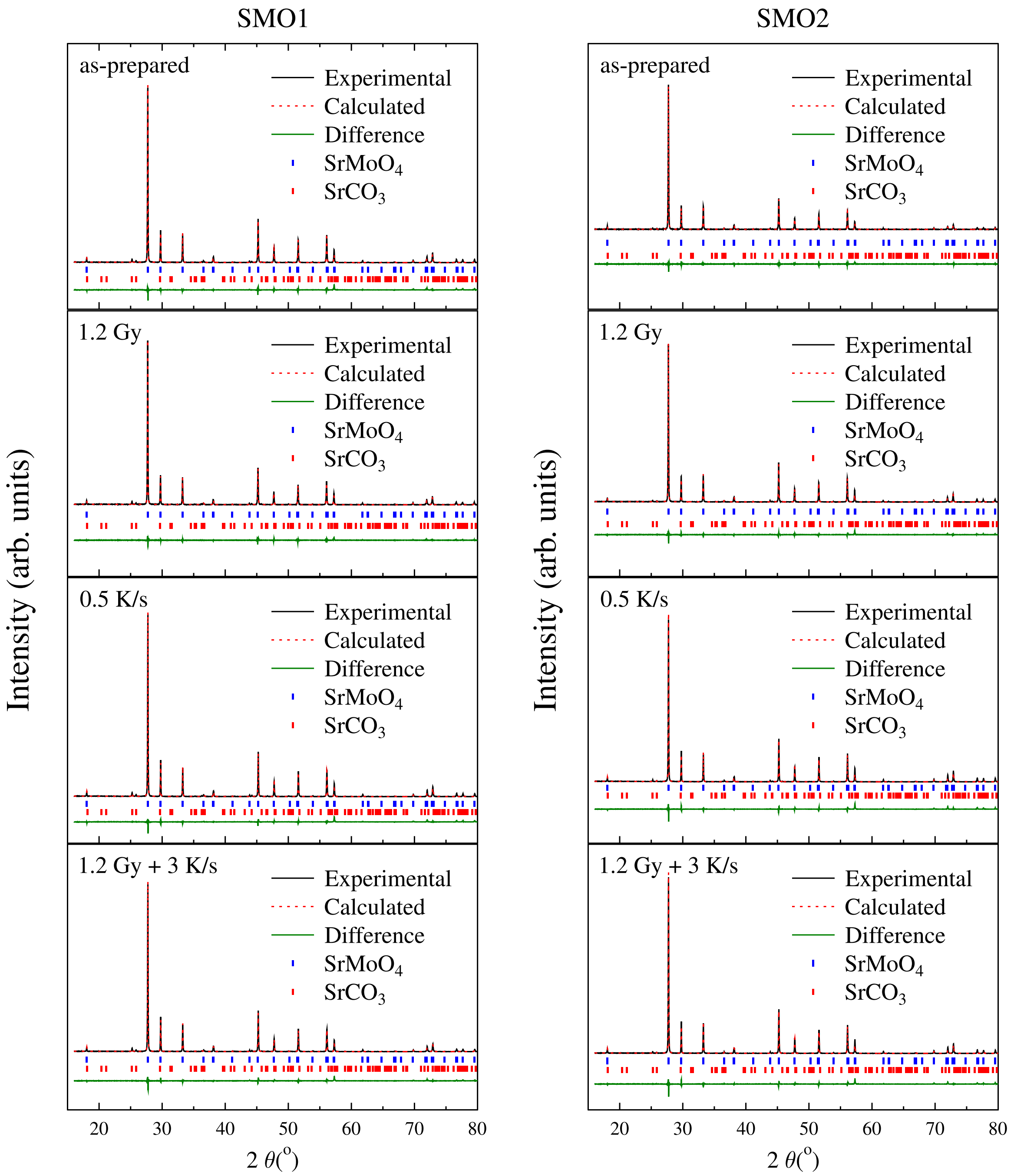

Fig. 2. XRD patterns and Rietveld refinements of the SMO1 and SMO2 samples subjected to different treatments and the Bragg peaks for $SrMoO_4$ (JCPDS No. 08-0482).

interstitial oxygen ions, and the more complicated structures such as defect clusters. Theoretical calculations from $CaWO_4$ materials, which have a similar crystalline structure to the $CaMoO_4$, reveal that the oxygen vacancy and interstitial oxygen defects, named Frenkel defects, have the lower formation energy and probably are the dominant defect type in the crystal [44,45]. Hence, the defects in the SMO1 and SMO2 structures could also be mainly related to Frenkel defect.

Fig. 3 displays the Raman and FTIR spectra employed to investigate the modifications on the material structure resulting from heating treatment and irradiation with beta particles. Each Raman band describes the vibration modes resulting from the scatter observed for periodically organized clusters and atoms in matter. The vibrational modes in Raman spectra of molybdates are classified into internal and external [9,13]. The internal vibration modes are associated with the tetrahedral $[MO_4]^{2-}$ cluster vibration in the lattice with a stationary mass center while the external modes are related to the motion of the Sr^{2+} cations, and the rigid molecular unit [9,13]. The observed internal Raman vibration modes are assigned to ν_1(Ag) (887 cm^{-1}), ν_3(Bg) (845 cm^{-1}), ν_3(Eg) (796 cm^{-1}), ν_4(Eg) (382 cm^{-1}), ν_4(Bg) (367 cm^{-1}) and ν_2(Bg) (328 cm^{-1}). The peak at 182 cm^{-1} corresponds to the free rotation mode. The observed lines in the range from 97–140 cm^{-1} are assigned to the external modes [9,13]. The registered Raman spectra (Fig. 3A and B) show that all the samples exhibit a single-crystalline phase with the scheelite-type tetragonal structure without phase modifications induced by the electrons irradiation and heating treatments. However, Raman and FTIR bands show a notable change in the intensity for the samples submitted to irradiation or heating treatment compared to the as-prepared samples.

The Raman modes frequencies remain nearly constant for all the SMO1 and SMO2 samples, and all the peaks are visible over the

Table 2
Lattice parameters, unit-cell volume, crystallite size and the mass fraction (wt%) of $SrMoO_4$ and $SrCO_3$ phases in the samples obtained by Rietveld refinement for the $SrMoO_4$ powders. The Eg parameter corresponds to the band gap energy calculated from UV–VIS experimental data.

	Sample	JCPDS No. 08–0482	as-prepared	1.2 Gy	1.2 Gy + 3 K/s	0.5 K/s
SMO1	Dcrys (nm)	–	225(12)	185(7)	194(9)	204(9)
	Eg (eV)	–	4.14(1)[a]	4.13(1)	4.15(1)	4.17(2)
	$SrMoO_4$(wt%)	–	96.30(9)	95.72(10)	96.03(8)	95.82(9)
	$SrCO_3$(wt%)	–	3.70(9)	4.28(10)	3.97(9)	4.18(9)
Lattice Parameters	a = b (Å)	5.394	5.38731(5)	5.38930(5)	5.38476(5)	5.38517(5)
	c (Å)	12.02	12.00700(14)	12.01158(13)	12.0084(13)	12.00144(13)
	c/a	2.228	2.229	2.229	2.228	2.228
	V (nm^3)	349.8	348.5	348.9	348.0	348.1
SMO2	Dcrys (nm)	–	131(5)	154(5)	174(7)	210(10)
	Eg (eV)	–	4.16(2)[a]	4.14(1)	4.18(4)	4.18(4)
	$SrMoO_4$(wt%)	–	98.59(9)	98.51(7)	98.38(7)	98.26(8)
	$SrCO_3$(wt%)	–	1.41(9)	1.49(7)	1.62(7)	1.74(8)
Lattice Parameters	a = b (Å)	5.394	5.38602(7)	5.38796(5)	5.38472(5)	5.38539(5)
	c (Å)	12.02	12.00436(19)	12.00892(13)	12.00046(13)	12.00212(13)
	c/a	2.228	2.229	2.229	2.229	2.229
	V (nm^3)	349.8	348.2	348.6	348.0	348.1

[a] Künzel et al. [17].

Table 3
Relative band height and measured FWHM values (cm^{-1}) for the main Raman bands in $SrMoO_4$ powders submitted to different post-synthesis treatments.

	Raman Band (cm^{-1})							
	887		845		796		328	
	Height	FWHM	Height	FWHM	Height	FWHM	Height	FWHM
SMO1								
as-prepared	1.0	4.56(0.1)	1.0	4.29(0.15)	1.0	5.02(0.10)	1.0	13.62(0.19)
1.2 Gy	1.05	4.81(0.11)	1.05	4.45(0.16)	1.03	5.03(0.15)	1.05	13.60(0.16)
1.2 Gy + 3 K/s	0.66	4.37(0.1)	0.70	3.96(0.1)	0.71	4.61(0.10)	0.62	12.90(0.16)
0.5 K/s	0.55	4.56(0.07)	0.59	4.08(0.08)	0.59	4.69(0.10)	0.51	13.20(0.15)
SMO2								
as-prepared	1.0	4.63(0.20)	1.0	4.21(0.23)	1.0	5.07(0.16)	1.0	13.40(0.21)
1.2 Gy	0.84	4.40(0.16)	0.90	4.13(0.18)	0.85	5.00(0.14)	0.86	13.29(0.22)
1.2 Gy + 3 K/s	0.80	4.40 (0.12)	0.84	3.94(0.11)	0.88	4.67(0.13)	0.78	13.10(0.19)
0.5 K/s	0.60	4.34 (0.12)	0.67	3.92(0.12)	0.66	4.67(0.14)	0.59	13.10(0.21)

whole measured spectrum 3. Raman spectroscopy is a valuable tool for investigating the structural order and disorder in materials. The first-order Raman phonon spectrum comprises narrow lines for a perfect crystal, and for disordered materials, broadened first-order Raman lines are observed [46]. The recorded spectra from $SrMoO_4$ powders can be ascribed to samples with disordered-ordered levels since they exhibit broad Raman bands indicating the phonon density of states correlated to the lattice expansion. The relative peaks intensity and FWHM (Full Width at Half Maximum) values of Raman bands for the prominent peaks were calculated and are depicted in Table 3. Considering that narrow lines are characteristics of an ordered crystal, the calculated FWHM values demonstrate that the studied materials have slightly different levels of defects. Results in Table 3 show that within the SMO1 sample set, the SMO1 - 1.2 Gy display the less ordered Raman spectrum, while for the SMO2 set, the less ordered spectrum refers to the as-prepared SMO2 powders. These observations agree with the Rietveld refinement analysis once the samples with the smaller crystallite size display the higher FWHM values indicating more disordered structures.

Fig. 3(C, D) compares the FTIR spectra from the as-prepared, irradiated, and submitted to heat treatment SMO1 and SMO2 samples. The spectra were registered in the range from 400 to 1000 cm^{-1}. The broad and intense absorption bands located between 800 and 900 cm^{-1} are assigned to the Mo-O stretching vibrations of the $[MoO_4]$ tetrahedron group [47]. The $\nu_3(F_2)$ symmetric (ν_s) and asymmetric (ν_{as}) stretch vibrations occur around 845 cm^{-1} and 803 cm^{-1}, respectively [48]. The band at 419 cm^{-1} is assigned to δ_{as} mode and the band at 404 cm^{-1} to $\nu_2(e)$ mode related to the $[MoO_4]^{-2}$ tetrahedron bending vibrations [48].

The FTIR spectra from SMO1 and SMO2 samples submitted to heat-treatment and irradiation show a slight shift in the frequency of $[MoO_4]^{2-}$ absorption band in comparison with the frequencies for the as-prepared sample. Table 4 presents the central frequency position for each band according to the adopted post-synthesis treatment. The vibration mode frequency modifications indicate that some bonds length was shortened observed through the shift of the phonon vibrations to higher frequencies while others were enhanced (shift to lower frequency vibration). The intensity of the FTIR bands depends on the square of the change in the dipole moment related to the vibrational amplitude [49,50]. Fig. 3(C, D) shows that the intensity of the absorption bands for the 1.2 Gy and heated SMO1 samples, with decreased crystallite size, increase compared to the as-prepared SMO1 sample, with a larger crystallite size. The intensity of the FTIR spectra from the 1.2 Gy and heated SMO2 samples, with increased crystallite size, decreases relative to the as-prepared SMO2 (smaller

Table 4
FTIR frequencies (cm^{-1}) observed in $SrMoO_4$ powders.

	FTIR bands (cm^{-1})			
	$\nu_3(s)$	$\nu_3(as)$	$\delta(as)$	$\nu_2(e)$
SMO1				
as-prepared	838	803	419	402
1.2 Gy	833	803	424	404
1.2 Gy + 3 K/s	835	803	419	403
0.5 K/s	835	803	418	403
SMO2				
as-prepared	847	804	423	403
1.2 Gy	844	806	419	404
1.2 Gy + 3 K/s	842	808	423	404
0.5 K/s	842	811	418	405

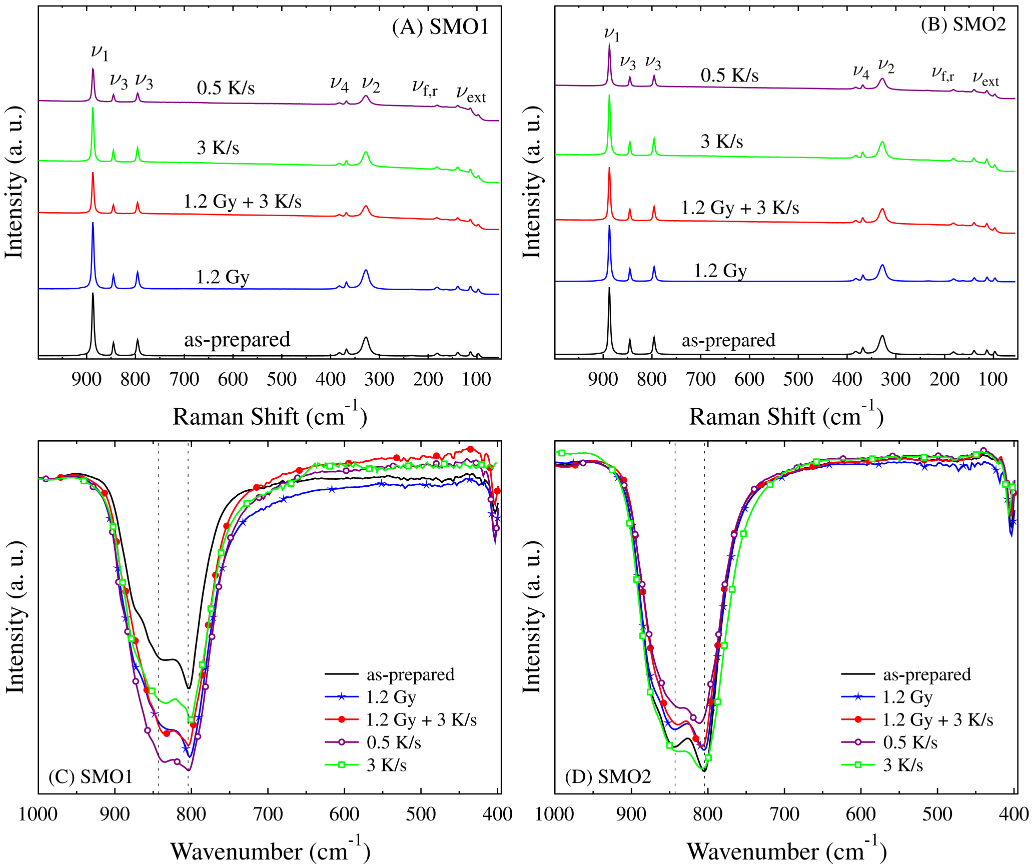

Fig. 3. Raman (A and B) and FTIR (C and D) spectra of SMO1 and SMO2 samples subjected to different treatments. The as-prepared samples are from Künzel et al. [17].

crystallite size). The irradiation of higher-ordered (as-prepared SMO1) induces the formation of defects, which increases material disorder. The opposite occurs in as-prepared SMO2, where these treatments increase the crystallite size and organization level, decreasing the intensity of FTIR bands.

3.2. Scanning and transmission electron microscopy

Fig. 4 illustrates the scanning electron microscopy (SEM) images at 10.000 x magnifications from as-prepared SMO1 and SMO2, and, after these samples were submitted to electron irradiation (1.2 Gy), irradiation followed by thermal treatment (1.2 Gy + 3 K/s) and only thermal treatment (0.5 K/s). Fig. 4 (A and B) correspond to as-prepared, (C and D) irradiated with 1.2 Gy, (E and F) to 1.2 Gy + 3 K/s, and (G and H) to the heating rate of 0.5 K/s, to SMO1 and SMO2 samples, respectively. All samples exhibit mainly octahedral morphologies, forming cauliflower-like $SrMoO_4$ structures, similar to those reported in previous works [9,17]. SEM images reveal the formation of small holes in the surface of the particle submitted to thermal treatments at 873 K when compared to the as-prepared SMO1 and SMO2 (Fig. 4(E-H)). These surface defects can be crucial in catalytic and photocatalytic processes; Materials with a large surface area are recommended for utilization in these processes due to the higher number of active sites available.

Fig. 5 display TEM images of $SrMoO_4$ crystals prepared by the co-precipitation method and exposed to beta particle irradiation (1.2 Gy) registered at 1 μm and 200 nm. TEM images confirm that the particles are highly agglomerated, showing some holes and brighter regions inside the same structure. The brighter regions within the particle surfaces, observed in the image registered at 200 nm, were also observed in other materials and are attributed to densification voids formed by coalescence of vacancies as the particles grow during the synthesis process [51]. The particle length distribution indicates that the particle size for this sample ranges over a large range with a mean value of 244 ± 83 nm. The selected area electron diffraction (SAED) pattern corresponds to powder diffraction from multiple crystals, showing both discrete spots and rings [52].

Fig. 6 shows TEM images from the 1.2 Gy SMO2 sample registered at 1 μm and 200 nm. The SMO2 samples also show high particle agglomeration, and the samples also display the densification voids of vacancies at a lower proportion compared to the SMO1 sample. These results indicate that the SMO2 sample presents a higher-order degree than the SMO1 sample. The particle length distribution, calculated with the ImageJ software, provides a means value of 211 ± 39 nm. The SAED patterns also reveal that SMO2 is polycrystalline.

3.3. Optical and magnetic properties

The absorbance for as-prepared, 1.2 Gy, 1.2 Gy + 3 K/s, and 0.5 K/s of the SMO1 and SMO2 powders were measured from 200 nm to 800 nm. The absorbance spectra, in wavelength units, were transformed to energy units using the Jacobian conversion method (Fig. 7) [34]. The registered data display a broadband with maximum intensity around 4.6 eV (261 nm), assigned to the electronic transitions of the $[MoO_4]^{2-}$ complex. The experimental band gap energies for SMO1 and SMO2 structures were estimated using the Wood and Tauc method according to the Kubelka Munk relationship as follows [36]:

$$h\nu\alpha \propto (h\nu - E_{gap})^n \tag{1}$$

where h is the Planck constant, ν is the photon frequency, α is the absorbance, E_{gap} is the optical band gap energy, and n is a constant associated with the type of electronic transition [53]. Table 2 brings the determined band gap values for the SMO1 and SMO2 samples. Results show a small variation, within the experimental uncertainties, on the

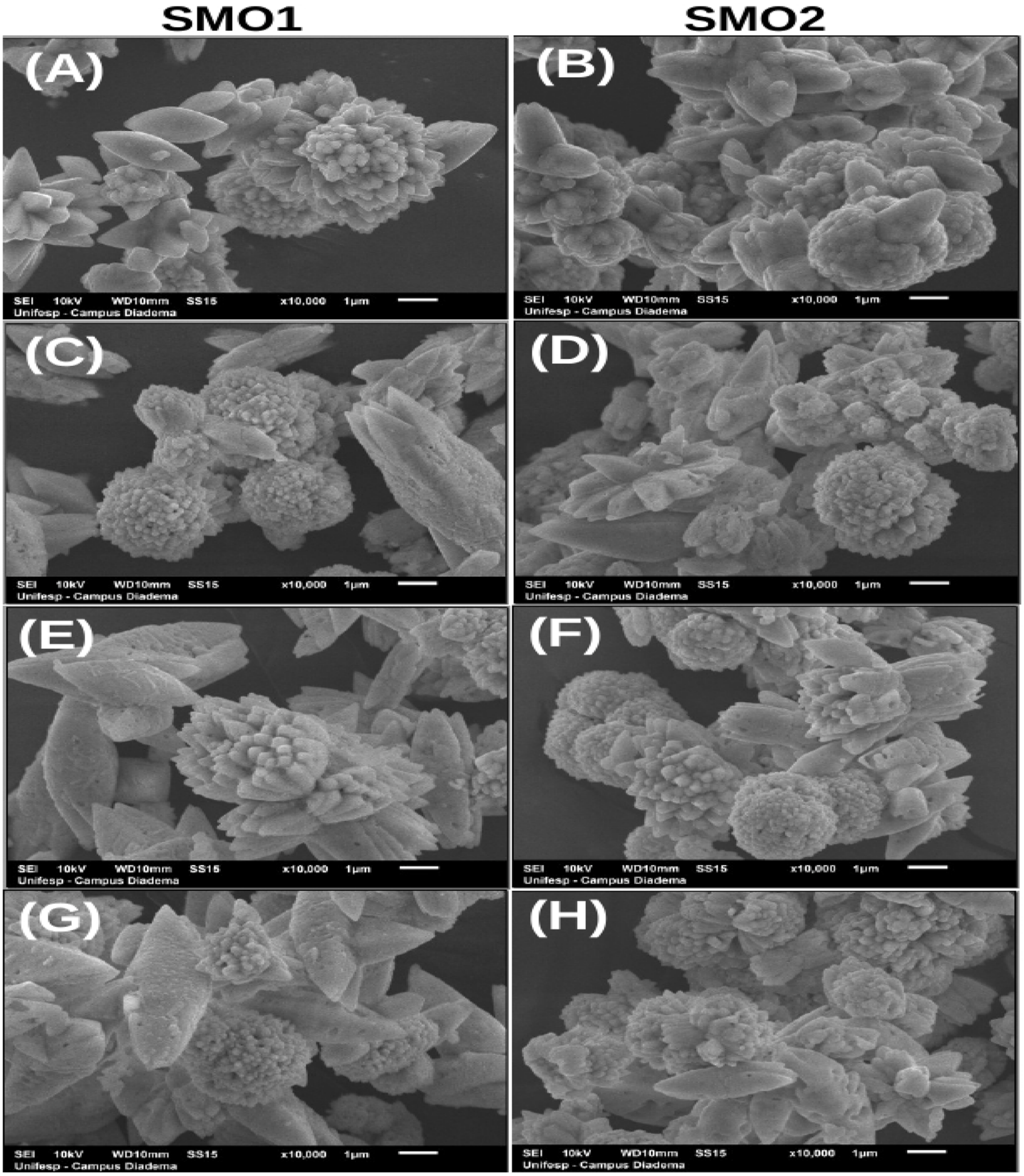

Fig. 4. SEM images from samples subjected to different treatments at 10000x magnification, where: (A) and (B) are as-prepared; (C) and (D) are 1.2 Gy; (E) and (F) are 1.2 Gy + 3 K/s; and (G) and (H) are 0.5 K/s to SMO1 and SMO2 samples, respectively.

band gap energy values with irradiation and heating treatment relative to the as-prepared sample. Fig. 7(C) illustrates the excitation spectra (PLE) of the as-prepared SMO1 and SMO2 samples, λ_{EM} = 459 nm at room temperature. In PLE, the two samples display a peak located in the range from 250 to 300 nm (4.96–4.13 eV), attributed to the charge transfer transition $O^{2-} \rightarrow Mo^{6+}$ due to the transition of a 2p electron of O^{2-} to the d orbital of Mo^{6+} [54], confirming the UV–Vis absorbance spectra data previously discussed. The PLE from the SMO1 sample display two additional peaks, one with a maximum at 325 nm (3.81 eV) and the other at 427 nm (2.9 eV). The SMO2 sample displays a broadband peaking at around 375 nm (3.31). These bands are attributed to intermediate energy levels inside the band gap of SMO1 and SMO2 compounds resulting from intrinsic defects generated during the synthesis methodology and the organization level promoted by the MHA treatment.

The photoluminescent emission (PL) spectra at room temperature, excited at 280 and 359 nm, from the SMO1 and SMO2 powders are shown in Fig. 8(A-D). The short wavelength PL emission from the samples, excited at 280 nm (4.42 eV), are mainly assigned to the electronic transitions from the complex $[MO_4]^{2-}$ structure and shallow defects structures [44]. The long-wavelength emission is assigned to the excitons captured by defect centers [44]. For all SMO1 and SMO2 samples, excited at 280 nm, the PL spectra consist of a predominantly emission band centering at 496 nm (Fig. 8(A-B)). Results also show that the samples subjected to heat treatment present a decreased PL intensity than the as-prepared and irradiated ones, indicating a modification of the material structure.

Fig. 8 (C-D) depicts the PL spectra from samples excited at 359 nm. The defects centers can be excited when the excitations photons energy are lower than the material band gap [55]. The PL emission, for 359 nm

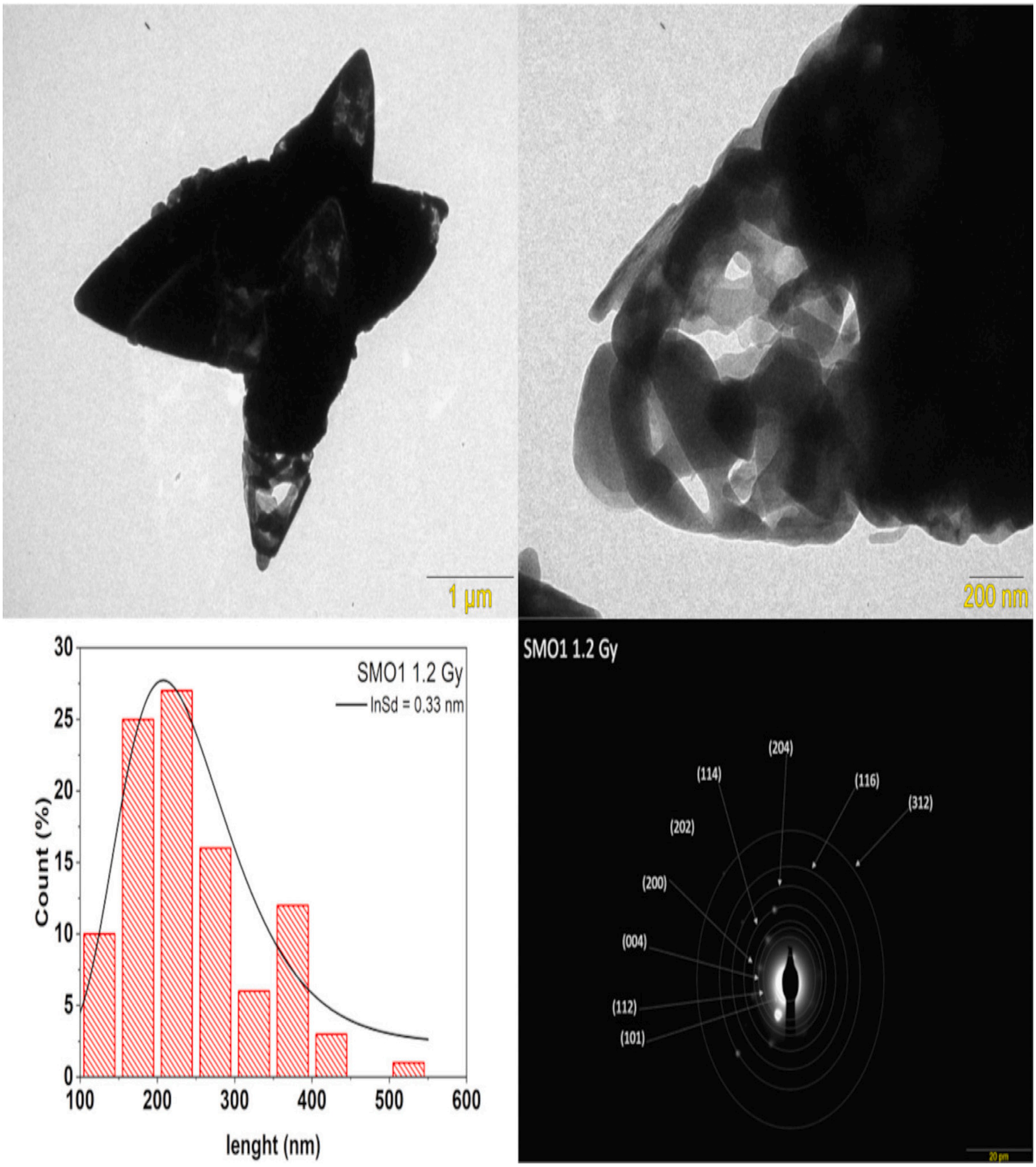

Fig. 5. TEM images from SMO1-1.2 Gy registered at 1 μm and 200 nm, the particle length distribution and SAED pattern.

excitation, present profile considerably different between samples. The observed peak profiles depend on synthesis methodology and the post-synthesis treatment and can be attributed to the direct excitation of the defect states located in the forbidden band of SMO1 and SMO2 samples. An additional defect level should probably induce the observed low-intensity band at the red-IR spectral region (around 620 nm) in the as-prepared SMO1 and SMO1 1.2 Gy samples. The observed variation in the PL spectra from the samples can be assigned to different levels of structural organization, oxygen vacancies, and defect clusters [46]. Results show a variation in the maximum peak emission for irradiated and heated samples compared to the as-prepared samples indicating different levels of order–disorder. The applied post-synthesis treatments are responsible for create or destroy some defects levels inside the band gap and induces variation on the defect levels distribution and density, affecting both the intensity and the maximum PL emission wavelength.

The magnetic properties of SMO1 and SMO2 powders, measured at 300 K, are shown in Fig. 9 (A and B) under a magnetic field ranging from −10 to +10 kOe. The data represents the magnetization (M) as a function of the applied magnetic field for as-prepared, heat-treated (1.2 Gy + 3 K/s and 0.5 K/s), and submitted to irradiation (1.2 Gy) SMO1 and SMO2 powders. The ferromagnetic response for some of the analyzed samples is observed from the S-shaped hysteresis loops in the low-field region. The as-prepared SMO1 sample, as depicted in Fig. 9 (A) and in its inset, displays a ferromagnetic behavior with a magnetic moment of 0.15 emu/g and 25 Oe coercive field. The SMO1 + 1.2 Gy sample shows a decreased ferromagnetic response, where the irradiation with 1.2 Gy dose from beta particles reduces the saturation moment magnetic to around 0.05 emu/g and a coercive field around 10 - 35 Oe. The M(H) curves show that the ferromagnetic response is suppressed for the SMO1 1.2 Gy + 3 K/s and SMO1 0.5 K/s powders, which show a linear M(H) performance with a low

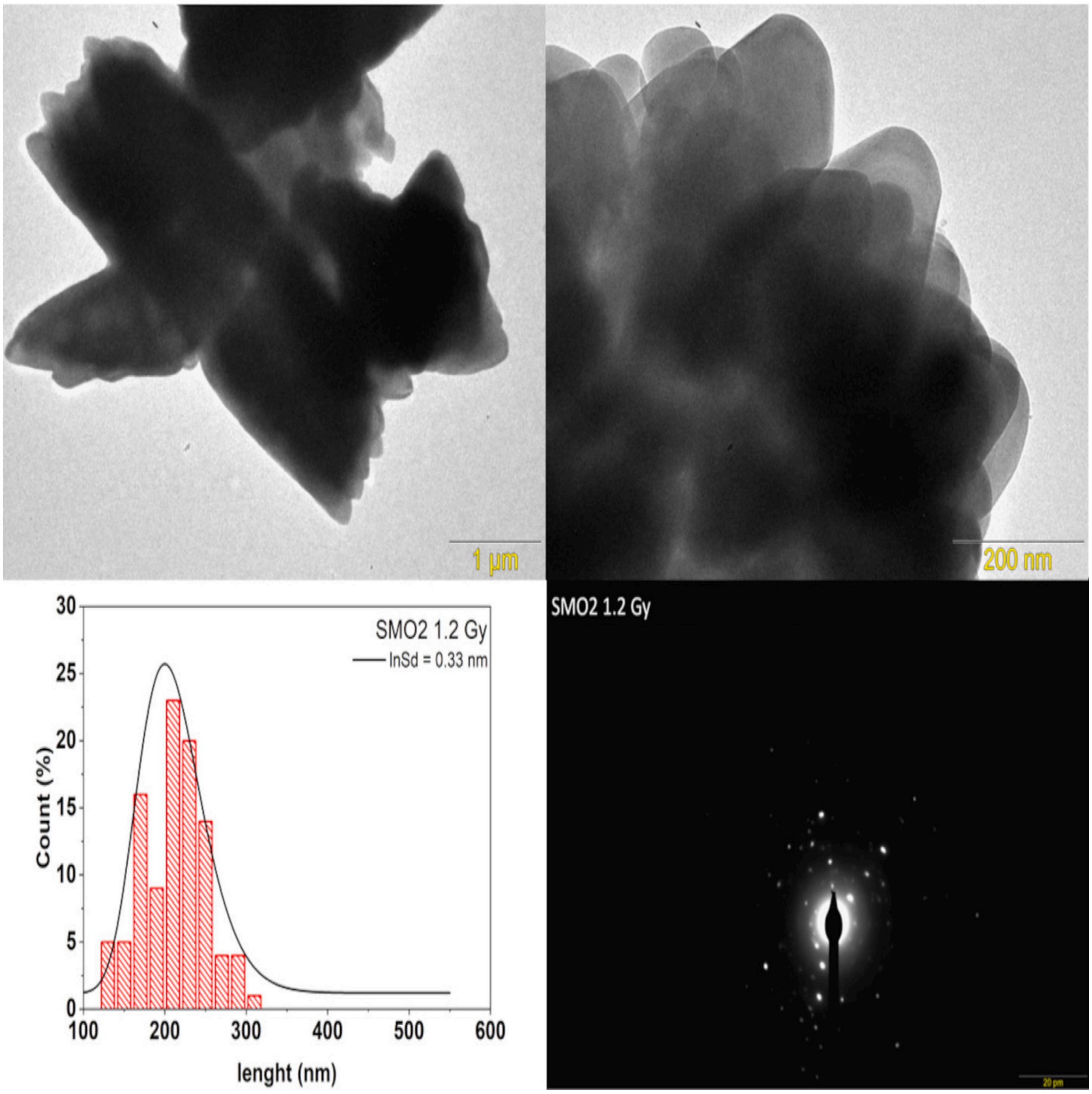

Fig. 6. TEM images from SMO2-1.2 Gy registered at 1 μm and 200 nm, the particle length distribution and SAED pattern.

magnetic moment, analogous to a paramagnetic response, as observed for undoped $SrMoO_4$ compounds [22]. The M(H) curve from the as-prepared SMO2 indicates a typical diamagnetic behavior. Here, we have ensured that the diamagnetic signal is from the sample and not an artifact of the sample loading. In fact, according to the literature [56], the diamagnetic contribution from the gelatin capsules and the plastic straws commonly used for mounting samples magnetization measurements are on the order of 10^{-4} emu/g. Since the diamagnetic signal measured for the as-prepared SMO2 sample is around 0.005 emu/g, we conclude that the observed diamagnetic behavior is, indeed, from the sample. For the SMO2 + 1.2 Gy sample, we observed a shift in magnetic behavior from diamagnetism to ferromagnetism with a saturation magnetic moment of around 0.005 emu/g and a coercive field of around 30 Oe. The observed ferromagnetism behavior in the SMO2 + 1.2 Gy powders can be attributed to modifications in the defect states induced by the irradiation with beta particles. The heating treatment switches the ferromagnetic behavior to diamagnetic again, as observed for the 1.2 Gy + 3 K/s sample. On the other side, the SMO2 + 0.5 K/s sample displays a paramagnetic response with the applied magnetic field.

The observed differences in the magnetic behavior from the SMO1 and SMO2 samples can be attributed to modifications in the material's structure induced by the hydrothermal treatment, the incidence of beta particles, and heating treatment. In a previous work published by our group [17] we presented thermoluminescence (TL) measurements from the as-prepared and irradiated SMO1 and SMO2 samples investigated in this work, and the outcomes give insights about modifications on the distribution and density of the trapping states in the examined materials. The observed results by Künzel et al. [17] show a symmetric distribution of the defects states in the as-prepared SMO1 sample. The irradiation of the SMO1 powders results in a decrease of the trap density without affecting the curve symmetry compared with the as-prepared SMO1 sample. The results suggest that this symmetric density distribution of the trapping states results in the ferromagnetic response of the as-prepared and 1.2 Gy SMO1 powders. In the case of the as-prepared SMO2 sample, which shows a diamagnetic behavior, the density of defects with lower trapping energy (around 1.18 eV) is about twice as high as the density of the deeper trapping states (trapping energy around 1.81 eV) [17]. The irradiation process with beta particles (1.2 Gy) reduces the density of the lower energy trapping states while the density of the deeper defects states remains almost unchanged. The SMO2 + 1.2 Gy sample, with a nearly symmetric density of defects states, shows the ferromagnetic behavior. Therefore,

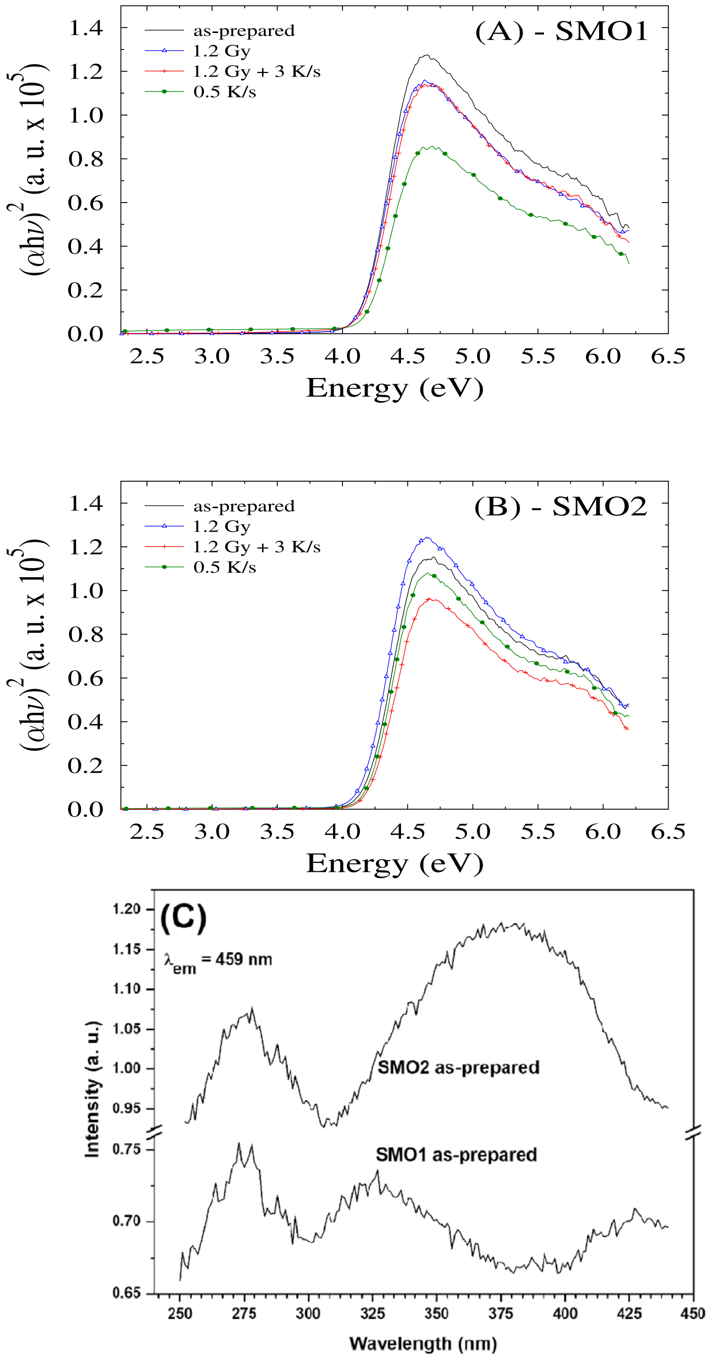

Fig. 7. Tauc plots from SMO1 (A) and SMO2 (B) samples as-prepared, 1.2 Gy, 1.2 Gy + 3 K/s and 0.5 K/s registered. The UV–VIS from as-prepared samples are from Künzel et al. [17]. (C) The photoluminescent excitation (PLE) spectra of as-prepared SMO1 and SMO2 samples (λ_{em} = 459 nm).

results indicate that deep defects such as oxygen vacancies may be necessary, but their distribution and density also affect the magnetism response in the $SrMoO_4$ compounds, in agreement with observations in other materials [23]. The 1.2 Gy + 3 K/s SMO2 sample shows that the thermal treatment suppressed the ferromagnetism response, and the sample evolved to diamagnetic again, which can be ascribed to the removal of deep defects and increased density of defects states with lower trapping energy. Therefore, a suitable combination of irradiation and thermal treatment can tune the magnetic behavior of $SrMoO_4$ compounds via the creation/removal of oxygen vacancies and modification of the trapping state's density and distribution. The observed difference in the magnetic behavior between each sample set (SMO1 or SMO2) can be attributed to an intrinsic phenomenon since the chemical composition and synthesis methodology is identical. The density and distribution of trapping states are tuned by synthesis methodology, heat treatment, and Irradiation processes and they affect the magnetic response of $SrMoO_4$. The outcomes of this work suggest that Irradiation with beta particles can be employed as an efficient processing tool to improve the optical and magnetic properties of $SrMoO_4$ phosphors.

4. Conclusion

In this work, $SrMoO_4$ nanostructures were synthesized by co-precipitation (SMO1) and co-precipitation followed by microwave-assisted hydrothermal (MAH) treatment (SMO2). The SMO1 and SMO2 samples were submitted to the following post-synthesis treatments: a)

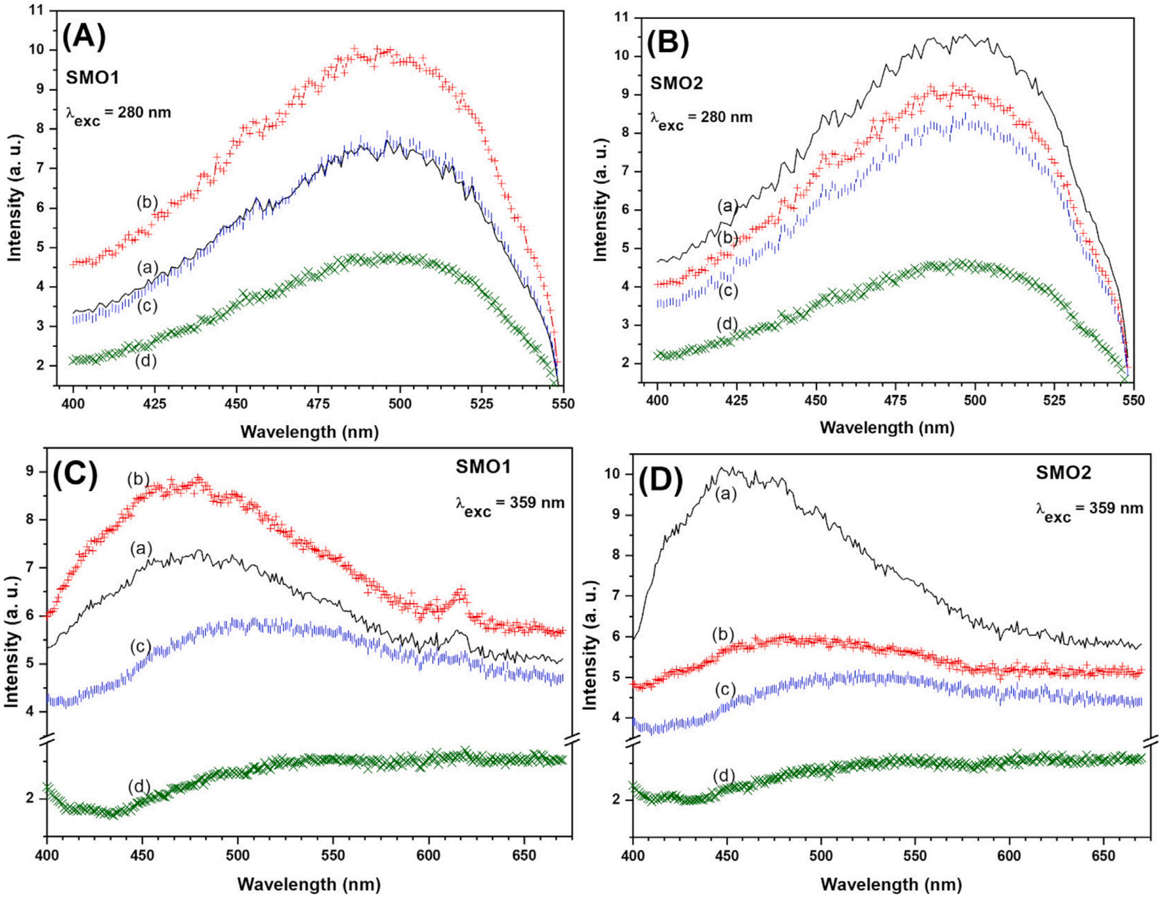

Fig. 8. The emission spectra (A and B) ($\lambda_{ex} = 280$ nm) and (C and D) ($\lambda_{ex} = 359$ nm) of SMO1 and SMO2 samples, where (a) = as-prepared; (b) = 1.2 Gy; (c) = 1.2 Gy + 3 K/s; and (d) = 0.5 K/s.

irradiation with beta particles (1.2 Gy), b) heat-treatment at 0.5 K/s until 873 K; and c) beta irradiation (1.2 Gy) followed to heat treatment at 3 K/s until 873 K. The characterization techniques, mainly XRD Rietveld refinement,TEM, Raman, and FTIR spectra, showed that the as-prepared SMO1 sample was more disordered than the as-prepared SMO2, where the higher-order was favored by the MHA treatment. The irradiation and heat treatment affected the as-prepared SMO1 and SMO2 in distinct ways without modifying the scheelite type crystalline phase. The irradiated SMO1 sample displays a more disordered structure than the as-prepared SMO1, while the irradiated SMO2 is more ordered than the as-prepared SMO2. The band gap energy values for the designed powders ranges from 4.13 to 4.18 eV. The registered PL intensity, at room temperature, under 280 nm and 359 nm excitation, can be directly related to the order–disorder of each sample. The PL emission was associated with the transitions in the tetrahedral $[MoO_4]^{2-}$ group as well as structural defects states. Magnetization results confirm the occurrence, at room temperature, of ferromagnetism for as-prepared SMO1 and SMO1 + 1.2 Gy samples were induced by deep trapping states such as oxygen vacancies, resulting in a magnetic moment of around 0.15 emu/g and 0.05 emu/g, respectively. The as-prepared SMO2 sample shows diamagnetic behavior while the irradiated (SMO2 + 1.2 Gy) powder presents a ferromagnetic response with a saturation magnetic moment of approximately 0.005 emu/g. The SMO2 samples return to a diamagnetic response after thermal treatment at 3 K/s until 873 K. The observed results reveal that the ferromagnetic order in SMO2 compounds depends on the density and distribution of the defect state. The coalescence of magnetic and optical features in the $SrMoO_4$ compounds demonstrates that the properties of the samples can be modulated by the synthesis methodology or by external influences, such as beta particle irradiation, making them suitable candidates for technological applications, for example, in optoelectronic devices.

Declaration of competing interest

The authors declare that they have no known competing financial interests or personal relationships that could have appeared to influence the work reported in this paper.

Data availability

No data was used for the research described in the article.

Acknowledgments

The authors are grateful to NIPE-Unifesp and CEM-UFABC for experimental support. We would like to thank the Electron Microscopy facilities at the Chemistry Institute (UNESP) for the TEM analyses. This study was partially supported by the Coordenação de Aperfeiçoamento de Pessoal de Nível Superior — Brazil (CAPES) — Finance Code 001; financial support from the Brazilian agencies Conselho Nacional de Desenvolvimento Científico e Tecnológico (CNPq) (304154/2005-9 and 305601/2019-9) and São Paulo Research Foundation (FAPESP) (#2016/20578-5, #2013/07437-5, #2010/16437-0).

Appendix A. Supplementary data

Supplementary material related to this article can be found online at https://doi.org/10.1016/j.jmmm.2022.169761.

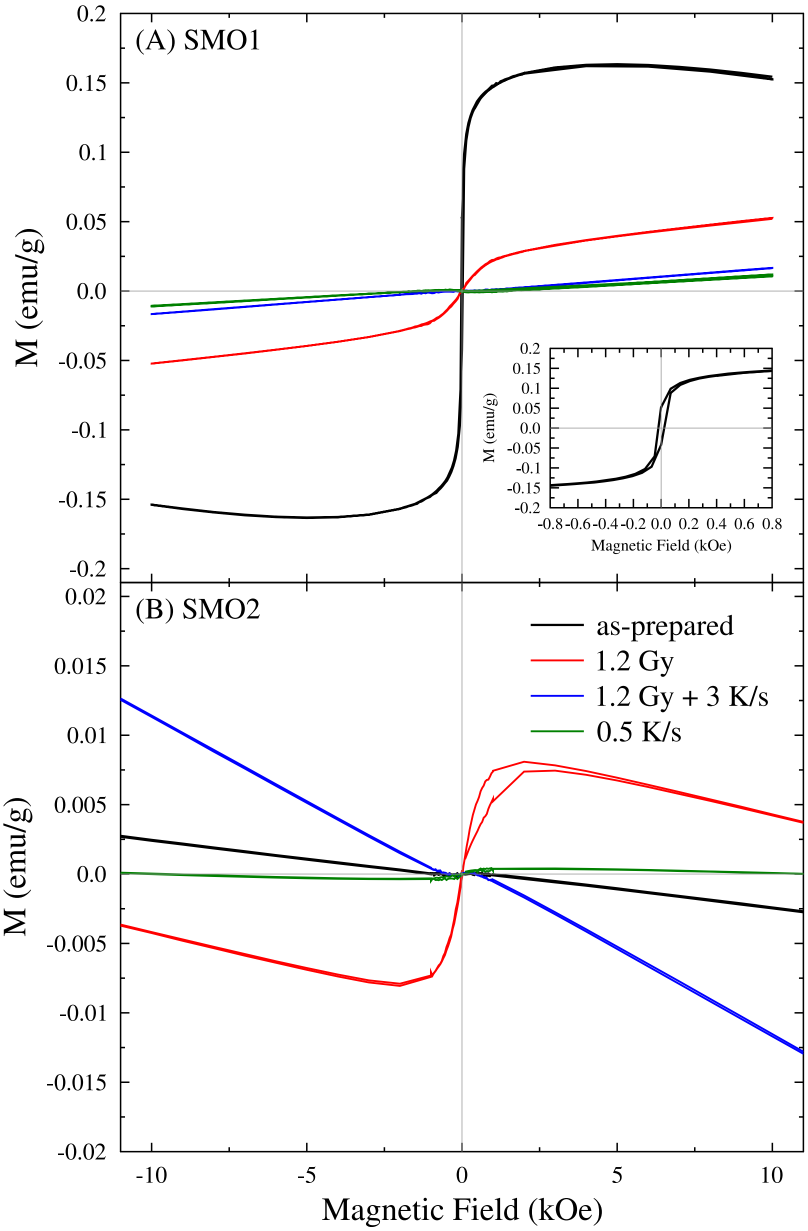

Fig. 9. Magnetization as a function of applied magnetic field (M × H) at 300 K from the as-prepared, 1.2 Gy, 1.2 + 3 K/s and the 0.5 K/s (A) SMO1 and (B) SMO2 powders.

References

[1] M. Maczka, A.S. Filho, W. Paraguassu, P. Freire, J.M. Filho, J. Hanuza, Pressure-induced structural phase transitions and amorphization in selected molybdates and tungstates, Prog. Mater. Sci. 57 (7) (2012) 1335–1381, http://dx.doi.org/10.1016/j.pmatsci.2012.01.001.

[2] Z.A. Mikhaylovskaya, E.S. Buyanova, S.A. Petrova, Sheelite-related strontium molybdates: synthesis and characterization, Chimica Techno Acta 5 (4) (2018) 189–195, http://dx.doi.org/10.15826/chimtech.2018.5.4.03.

[3] D. Errandonea, R.S. Kumar, X. Ma, C. Tu, High-pressure X-ray diffraction study of $SrMoO_4$ and pressure-induced structural changes, J. Solid State Chem. 181 (2) (2008) 355–364, http://dx.doi.org/10.1016/j.jssc.2007.12.010.

[4] M. Benzineb, F. Chiker, H. Khachai, H. Meradji, Uğur, S. Naqib, S.B. Omran, X. Wang, R. Khenata, A comparative study of structural, thermal, and optoelectronic properties between zircon and scheelite type structures in $SrMoO_4$ compound: An ab-initio study, Optik 238 (2021) 166714, http://dx.doi.org/10.1016/j.ijleo.2021.166714.

[5] F. Liu, J. Wang, L. Jiang, R. You, Q. Wang, C. Wang, Z. Lin, Z. Yang, J. He, A. Liu, P. Sun, X. Yan, G. Lu, Compact and planar type rapid response ppb-level SO_2 sensor based on stabilized zirconia and $SrMoO_4$ sensing electrode, Sensors Actuators B 307 (2020) 127655, http://dx.doi.org/10.1016/j.snb.2020.127655.

[6] E. Çiftyürek, K. Sabolsky, E. Sabolsky, Molybdenum and tungsten oxide based gas sensors for high temperature detection of environmentally hazardous sulfur species, Sensors Actuators B 237 (2016) 262–274, http://dx.doi.org/10.1016/j.snb.2016.06.071.

[7] H. Gao, C. Yu, Y. Wang, S. Wang, H. Yang, F. Wang, S. Tang, Z. Yi, D. Li, A novel photoluminescence phenomenon in a $SrMoO_4$/$SrWO_4$ micro/nano heterojunction phosphors obtained by the polyacrylamide gel method combined with low temperature calcination technology, J. Lumin. 243 (2022) 118660, http://dx.doi.org/10.1016/j.jlumin.2021.118660.

[8] D.F.D. Santos, L.X. Lovisa, A.A.G. Santiago, M.S. Li, E. Longo, M.R.D. Bomio, F.V. Motta, Growth mechanism and vibrational and optical properties of $SrMoO_4$: Tb^{3+}, Sm3 particles: green–orange tunable color, J. Mater. Sci. 55 (20) (2020) 8610–8629, http://dx.doi.org/10.1007/s10853-020-04623-5.

[9] S. Paradelas, R. Gonçalves, F.V. Motta, R.C. Lima, M. Li, E. Longo, A.P. de A. Marques, Effects of microwave-assisted hydrothermal treatment and of use of capping reagent on the photophysical properties of $SrMoO_4$ phosphors, J. Lumin 192 (2017) 818–826, http://dx.doi.org/10.1016/j.jlumin.2017.08.016.

[10] S. Swathi, R. Yuvakkumar, P.S. Kumar, G. Ravi, D. Nanthini, D. Velauthapillai, Flower like strontium molybdate for efficient energy conversion applications, Fuel 308 (2022) 122051, http://dx.doi.org/10.1016/j.fuel.2021.122051.

[11] S. Arai, T. Noguchi, T. Aida, A. Yoko, T. Tomai, T. Adschiri, M. Koshimizu, Y. Fujimoto, K. Asai, Development of liquid scintillators loaded with alkaline earth molybdate nanoparticles for detection of neutrinoless double-beta decay, J. Ceram. Soc. Japan 127 (1) (2019) 28–34, http://dx.doi.org/10.2109/jcersj2.18146.

[12] V. Mikhailik, Y. Elyashevskyi, H. Kraus, H. Kim, V. Kapustianyk, M. Panasyuk, Temperature dependence of scintillation properties of $SrMoO_4$, Nucl. Instrum. Methods Phys. Res. A 792 (2015) 1–5, http://dx.doi.org/10.1016/j.nima.2015.04.018.

[13] J. Sczancoski, L. Cavalcante, M. Joya, J. Varela, P. Pizani, E. Longo, $SrMoO_4$ powders processed in microwave-hydrothermal: Synthesis, characterization and optical properties, Chem. Eng. J. 140 (2008) 632–637, http://dx.doi.org/10.1016/j.cej.2008.01.015.

[14] V.M. Longo, A.T. de Figueiredo, A.B. Campos, J.W.M. Espinosa, A.C. Hernandes, C.A. Taft, J.R. Sambrano, J.A. Varela, E. Longo, Different origins of green-light photoluminescence emission in structurally ordered and disordered powders of calcium molybdate†, J. Phys. Chem. A 112 (38) (2008) 8920–8928, http://dx.doi.org/10.1021/jp801587w.

[15] A. Marques, D. Melo, C. Paskocimas, P. Pizani, E. Leite, E. Longo, in: A.M. Newman (Ed.), Study of the Photoluminescence $SrMoO_4$ Powders Synthesized by Complex Polymerization Method (CPM), first ed., in: Focus on Solid State Chemistry, Nova Science Publishers, Inc, Hauppauge NY, 2006.

[16] J. Sczancoski, L. Cavalcante, N. Marana, R. da Silva, R. Tranquilin, M. Joya, P. Pizani, J. Varela, J. Sambrano, M.S. Li, E. Longo, J. Andrés, Electronic structure and optical properties of $BaMoO_4$ powders, Curr. Appl. Phys. 10 (2) (2010) 614–624, http://dx.doi.org/10.1016/j.cap.2009.08.006.

[17] R. Künzel, N.K. Umisedo, E. Okuno, E.M. Yoshimura, A.P. de Azevedo Marques, Effects of microwave-assisted hydrothermal treatment and beta particles irradiation on the thermoluminescence and optically stimulated luminescence of $SrMoO_4$ powders, Ceram. Int. 46 (10) (2020) 15018–15026, http://dx.doi.org/10.1016/j.ceramint.2020.03.032.

[18] I.I. Lungu, A.M. Grumezescu, C. Fleaca, Unexpected ferromagnetism—A review, Appl. Sci. 11 (15) (2021) 6707, http://dx.doi.org/10.3390/app11156707.

[19] A. Sundaresan, C. Rao, Ferromagnetism as a universal feature of inorganic nanoparticles, Nano Today 4 (1) (2009) 96–106, http://dx.doi.org/10.1016/j.nantod.2008.10.002.

[20] M. Valant, T. Kolodiazhnyi, I. Arčon, F. Aguesse, A.-K. Axelsson, N.M. Alford, The origin of magnetism in mn-doped $SrTiO_3$, Adv. Funct. Mater. 22 (10) (2012) 2114–2122, http://dx.doi.org/10.1002/adfm.201102482.

[21] S. Qin, D. Liu, Z. Zuo, Y. Sang, X. Zhang, F. Zheng, H. Liu, X.-G. Xu, UV-irradiation-enhanced ferromagnetism in $BaTiO_3$, J. Phys. Chem. Lett. 1 (1) (2009) 238–241, http://dx.doi.org/10.1021/jz900131x.

[22] M. Muralidharan, V. Anbarasu, A.E. Perumal, K. Sivakumar, Enhanced ferromagnetism in Cr doped $SrMoO_4$ scheelite structured compounds, J. Mater. Sci.: Mater Electron. 27 (3) (2016) 2545–2556, http://dx.doi.org/10.1007/s10854-015-4057-1.

[23] P.D. Esquinazi, W. Hergert, M. Stiller, L. Botsch, H. Ohldag, D. Spemann, M. Hoffmann, W.A. Adeagbo, A. Chassé, S.K. Nayak, H.B. Hamed, Defect-induced magnetism in nonmagnetic oxides: Basic principles, experimental evidence, and possible devices with ZnO and TiO_2, Phys. Status Solidi (B) 257 (7) (2020) 1900623, http://dx.doi.org/10.1002/pssb.201900623.

[24] R. Singh, Unexpected magnetism in nanomaterials, J. Magn. Magn. Mater. 346 (2013) 58–73, http://dx.doi.org/10.1016/j.jmmm.2013.07.005.

[25] M. Muralidharan, K. Sivaji, Vacancy induced ferromagnetism in $SrWO_4$ and $SrMoO_4$ nano structured compounds, in: Dae Solid State Physics Symposium 2019, AIP Publishing, 2020, http://dx.doi.org/10.1063/5.0017336.

[26] S.M. Hosseinpour-mashkani, A. Sobhani-Nasab, M. Mehrzad, Controlling the synthesis $SrMoO_4$ nanostructures and investigation its photocatalyst application, J. Mater. Sci., Mater. Electron. 27 (6) (2016) 5758–5763, http://dx.doi.org/10.1007/s10854-016-4489-2.

[27] D. Guo, Q. Yang, H. Hua, C. Hu, Room temperature ferromagnetism in shuttle-like $BaMoO_4$ microcrystals, J. Phys. Chem. C 118 (25) (2014) 13826–13832, http://dx.doi.org/10.1021/jp504429g.

[28] H.M. Rietveld, A profile refinement method for nuclear and magnetic structures, J. Appl. Crystallogr. 2 (2) (1969) 65–71, http://dx.doi.org/10.1107/s0021889869006558.

[29] A.C. Larson, R.B.V. Dreele, General structure analysis system (gsas), Los Alamos National Laboratory Report LAUR, 2004, pp. 86–748.

[30] G. Sombrio, Z. Zhang, A. Bonadio, L.S. de Oliveira, T.B. de Queiroz, F.F. Ferreira, A. Janotti, J.A. Souza, Charge transport in $MAPbI_3$ pellets across the tetragonal-to-cubic phase transition: The role of grain boundaries from structural, electrical, and optical characterizations, J. Phys. Chem. C 124 (20) (2020) 10793–10803, http://dx.doi.org/10.1021/acs.jpcc.0c00887.

[31] A. Coelho, Topas and TOPAS-academic: an optimization program integrating computer algebra and crystallographic objects written in $C++$, J. Appl. Crystallogr. 51 (1) (2018) 210–218, http://dx.doi.org/10.1107/S1600576718000183.

[32] P. Scardi, Diffraction line profiles in the Rietveld method, Cryst. Growth Des. 20 (2020) 6903–6916, http://dx.doi.org/10.1021/acs.cgd.0c00956.

[33] A. Coelho, Topas, TOPAS-academic - technical reference V7, Tech. rep., Coelho Software, Brisbane, Australia, 2020, p. 266, [Online] URL http://www.topas-academic.net/Technical_Reference.pdf.

[34] J. Mooney, P. Kambhampati, Get the basics right: Jacobian conversion of wavelength and energy scales for quantitative analysis of emission spectra, J. Phys. Chem. Lett. 4 (19) (2013) 3316–3318, http://dx.doi.org/10.1021/jz401508t.

[35] V. Kolobanov, I. Kamenskikh, V. Mikhailin, I. Shpinkov, D. Spassky, B. Zadneprovsky, L. Potkin, G. Zimmerer, Optical and luminescent properties of anisotropic tungstate crystals, Nucl. Instr. and Meth. A 486 (2002) 496–503, http://dx.doi.org/10.1016/S0168-9002(02)00760-X.

[36] D. Wood, J. Tauc, Weak absorption tails in amorphous semiconductors, Phys. Rev. B: Condens. Matter. 5 (8) (1972) 3144–3151, http://dx.doi.org/10.1103/PhysRevB.5.3144.

[37] C.H. R. Hill, Quantitative phase-analysis from neutron powder diffraction data using the Rietveld method, J. Appl. Crystallogr. 20 (1987) 467–474, http://dx.doi.org/10.1107/S0021889887086199.

[38] S. Ni, X. Yang, T. Li, Hydrothermal synthesis and photoluminescence properties of $SrCO_3$, Mater. Lett. 65 (4) (2011) 766–768, http://dx.doi.org/10.1016/j.matlet.2010.11.056.

[39] P. Lu, X. Hu, Y. Li, M. Zhang, X. Liu, Y. He, F. Dong, M. Fu, Z. Zhang, One-step preparation of a novel $SrCO_3$/g-C_3 N_4 nano-composite and its application in selective adsorption of crystal violet, RSC Adv. 8 (12) (2018) 6315–6325, http://dx.doi.org/10.1039/c7ra11565b.

[40] J. Baltrusaitis, J. Schuttlefield, E. Zeitler, V.H. Grassian, Carbon dioxide adsorption on oxide nanoparticle surfaces, Chem. Eng. J. 170 (2–3) (2011) 471–481, http://dx.doi.org/10.1016/j.cej.2010.12.041.

[41] D.S. Cruz-Navarro, V. Mugica-Álvarez, M. Gutiérrez-Arzaluz, M. Torres-Rodríguez, 10, (3) 2020, p. 863, http://dx.doi.org/10.3390/app10030863.

[42] X. Wang, X. Ma, V. Schwartz, J.C. Clark, S.H. Overbury, S. Zhao, X. Xu, C. Song, A solid molecular basket sorbent for CO_2 capture from gas streams with low CO_2 concentration under ambient conditions, Phys. Chem. Chem. Phys. 14 (4) (2012) 1485–1492, http://dx.doi.org/10.1039/c1cp23366a.

[43] C.B. Carter, M.G. Norton, Sintering and grain growth, in: Ceramic Materials, Springer New York, pp. 427–443, http://dx.doi.org/10.1007/978-0-387-46271-4_24.

[44] Y. Li, Z. Wang, L. Sun, Z. Wang, S. Wang, X. Liu, Y. Wang, Investigation of oxygen vacancy and photoluminescence in calcium tungstate nanophosphors with different particle sizes, Mater. Res. Bull. 50 (2014) 36–41, http://dx.doi.org/10.1016/j.materresbull.2013.10.022.

[45] Z. Shao, Q. Zhang, T. Liu, J. Chen, Computer study of intrinsic defects in $CaWO_4$, Nucl. Instrum. Methods Phys. Res. B 266 (5) (2008) 797–801, http://dx.doi.org/10.1016/j.nimb.2008.01.018.

[46] M.F.C. Abreu, F.V. Motta, R.C. Lima, M.S. Li, E. Longo, A.P. de A. Marques, Effect of process parameters on photophysical properties and barium molybdate phosphors characteristics, Ceram. Int. 40 (5) (2014) 6719–6729, http://dx.doi.org/10.1016/j.ceramint.2013.11.134.

[47] T. Thongtem, S. Kungwankunakorn, B. Kuntalue, A. Phuruangrat, S. Thongtem, Luminescence and absorbance of highly crystalline $CaMoO_4$, $SrMoO_4$, $CaWO_4$ and $SrWO_4$ nanoparticles synthesized by co-precipitation method at room temperature, J. Alloys Compd. 506 (1) (2010) 475–481, http://dx.doi.org/10.1016/j.jallcom.2010.07.033.

[48] G.M. Clark, W.P. Doyle, Infra-red spectra of anhydrous molybdates and tungstates, Spectrochim. Acta A 22 (8) (1966) 1441–1447, http://dx.doi.org/10.1016/0371-1951(66)80137-6.

[49] P. Larkin, Infrared and Raman Spectroscopy; Principles and Spectral Interpretation, Elsevier, Amsterdam, 2011.

[50] D. Steele, The absolute intensities of infrared absorption bands, Q. Rev. Chem. Soc. 18 (1) (1964) 21, http://dx.doi.org/10.1039/qr9641800021.

[51] M. Minakshi, D.R.G. Mitchell, C. Baur, J. Chable, A.J. Barlow, M. Fichtner, A. Banerjee, S. Chakraborty, R. Ahuja, Phase evolution in calcium molybdate nanoparticles as a function of synthesis temperature and its electrochemical effect on energy storage, Nanoscale Adv. 1 (2) (2019) 565–580, http://dx.doi.org/10.1039/c8na00156a.

[52] R. Egerton, Physical Principles of Electron Microscopy: An Introduction to TEM, SEM, and AEM, Springer, New York, 2005.

[53] E.E. Dunaeva, P.G. Zverev, M.E. Doroshenko, A.V. Nekhoroshikh, L.I. Ivleva, V.V. Osiko, Growth and spectral-luminescent study of $SrMoO_4$ crystals doped with Tm^{3+} ions, Doklady Phys. 61 (3) (2016) 119–123, http://dx.doi.org/10.1134/s1028335816030058.

[54] W. Bi, Q. Meng, W. Sun, Luminescent properties and energy transfer mechanism of $NaGd(MoO_4)_2$:Sm^{3+}, Eu^{3+} phosphors, Ceram. Int. 42 (12) (2016) 14086–14093, http://dx.doi.org/10.1016/j.ceramint.2016.06.017.

[55] N. Ahmed, H. Kraus, H. Kim, V. Mokina, V. Tsiumra, A. Wagner, Y. Zhydachevskyy, V. Mykhaylyk, Characterisation of tungstate and molybdate crystals ABO_4 (A= Ca, Sr, Zn, Cd, B=W, Mo) for luminescence lifetime cryothermometry, Materialia 4 (2018) 287–296, http://dx.doi.org/10.1016/j.mtla.2018.09.039.

[56] M.A. Garcia, E.F. Pinel, J. de la Venta, A. Quesada, V. Bouzas, J.F. Fernández, J.J. Romero, M.S.M. González, J.L. Costa-Krämer, Sources of experimental errors in the observation of nanoscale magnetism, J. Appl. Phys. 105 (1) (2009) 013925, http://dx.doi.org/10.1063/1.3060808.